Sixth International Symposium on Turbulence and Shear Flow Phenomena
Seoul, Korea, 22-24 June 2009

ANALYSIS OF THE CLOUD-TOP MIXING LAYER USING DNS

Juan Pedro Mellado
Institute für Technische Verbrennung, RWTH Aachen,
Templergraben 64, 52056 Aachen, Germany,
jpmellado@itv.rwth-aachen.de

Heiko Schmidt
Zuse Institute, FU Berlin,
Takustr. 9, 14195 Berlin, Germany
heischmi@mi.fu-berlin.de
Bjorn Stevens
The Atmosphere in the Earth System, MPI for Meteorology
Bundesstr. 53, 20146 Hamburg, Germany
bstevens@atmos.ucla.edu
Norbert Peters
Institute für Technische Verbrennung, RWTH Aachen,
Templergraben 64, 52056 Aachen, Germany,
n.peters@itv.rwth-aachen.de

ABSTRACT

Direct numerical simulation is used to study the cloud-top mixing layer. This two-layer system models the mixing region that forms at stratocumulus tops when the upper warm and dry air mixes with the lower cloud, and one of its main features is that buoyancy reversal may appear due to evaporative cooling under certain conditions. First, the two-fluid formulation employed in the analysis is discussed, identifying the limitations of such an approach to handle the physics of the cloud. The buoyancy reversal instability that develops in the two-layer system is then presented, two-dimensional single-mode simulations showing the nonlinear regime of that instability and suggesting a possible turbulent regime in the lower layer. Three-dimensional simulations confirm that turbulent state. This turbulent flow is described in this paper using visualizations and statistics of the mixture fraction and the turbulent kinetic energy.

INTRODUCTION

It has been long recognized that cloud effects remain one of the largest sources of uncertainty in model-based estimates of climate sensitivity, and in particular entrainment rates in stratocumulus-topped mixed layers need urgently better models (Stevens, 2002) in order to improve predictions obtained with both large-eddy simulations or Reynolds averaged Navier-Stokes equations.

Stratocumulus-topped boundary layers, and specifically the possibility of an entrainment instability appearing at the top of the cloud deck due to buoyancy reversal created by evaporative cooling when the upper subsiding air mixes with the lower moist and cooler layer, have received considerable attention (Randall, 1980; Kuo and Schubert, 1988; Yamaguchi and Randall, 2008; Kurowski et al., 2009). Small-domain analyses via laboratory experiments and numerical simulations have been also reported (Shy and Breidenthal, 1990; Siems et al., 1990; Siems and Bretherton, 1992), and the linear stability analysis showing the buoyancy reversal instability of the cloud-top mixing layer has been recently derived (Mellado et al., 2009).

We present in this paper further results from the study of the shear-free cloud-top mixing layer using direct numerical simulation (DNS), with emphasis on the three-dimensional turbulent case. The *cloud-top mixing layer* is an idealized configuration defined by two unbounded horizontal layers, with the upper nonturbulent half-space warmer and unsaturated and the lower one, also nonturbulent, cooler and saturated (condensate laden), gravity acting downwards. It corresponds to length-scales of the order of 10 m, the typical size of the zone where turbulent entrainment concentrates (Caughey et al., 1982). The objective of the work is to gain understanding of part of the phenomena occurring at the cloud top, namely, latent heat effects, and ultimately to use the new results to derive better entrainment models or improved subgrid-scale closures. It needs to be distinguished from the stratocumulus-topped boundary layer (Lilly, 1968; Stevens, 2002), in which the finite-size bottom region is turbulent and its size is of the order of 10^3 m.

FORMULATION

Clouds involve simultaneously several complex physical phenomena, which makes understanding them a daunting task, and different simplifications are commonly adopted to make the problem more tractable (Shaw, 2003). In the context of cloud tops, a physical model based on a mixture fraction formulation (Bretherton, 1987) has been often employed and will be also used here. There are two major hypothesis underlying this approach. The first main assumption is that cloud droplets are small enough for a two-fluid formulation to be appropriate, and, in addition, small enough for a Brownian diffusion of the liquid phase to be dominant over the terminal velocity due to the gravity acceleration and with a diffusivity comparable to the vapor diffusivity. That is certainly not the case at stratocumulus tops, where the mean droplet diameter is reported to be about 10 μm, but the simplifications are enormous because the transport equations for enthalpy and total-water specific humidity are then simply advection-diffusion equations in the small-domain, low Mach number case that we con-

sider. The two-layer configuration allows to introduce then a mixture fraction $\chi(\mathbf{x},t)$ that represents the amount of mass in the fluid particle that originates from the upper layer, i.e. $\chi=1$ represents pure fluid from the upper layer and $\chi=0$ from the cloud below. Consequently, flow variables from the upper layer will be denoted by the subscript 1, and subscript 0 will correspond to the lower layer. The relative variations of density ρ are also small, less than 5%, and therefore the Boussinesq approximation proves to be valid, which leads to the system

$$\begin{aligned}\frac{\partial \mathbf{v}}{\partial t}+\nabla\cdot(\mathbf{v}\otimes\mathbf{v}) &= -\nabla p+\nu\nabla^2\mathbf{v}+b\mathbf{k}\\ \nabla\cdot\mathbf{v} &= 0\\ \frac{\partial \chi}{\partial t}+\nabla\cdot(\mathbf{v}\chi) &= \kappa\nabla^2\chi\end{aligned} \tag{1}$$

with the buoyancy defined by

$$b=\frac{\rho_0-\rho}{\rho_0}g \tag{2}$$

In the equations above, p is a modified pressure divided by the reference density ρ_0, the kinematic viscosity is ν, κ is the scalar diffusivity, g represents the (constant) magnitude of the gravity acceleration, and $\mathbf{k}$ is the unit vector along the vertical direction Oz.

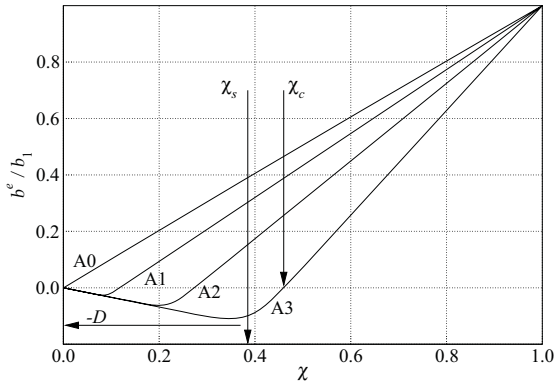

Figure 1: Nondimensional buoyancy mixing function for the cases presented in Table 1. Parameters D, χ_s and χ_c correspond to case A3.

The second main hypothesis consists in assuming thermodynamic equilibrium, so that the complete thermodynamic state of the fluid particle can be determined for a given χ, once a pressure level is prescribed. In particular, it provides the density and therefore the buoyancy term by $b(\mathbf{x},t)=b^e(\chi(\mathbf{x},t))$, which is a nonlinear function due to the phase transition of the water. For the small density variations occurring in the problem, it can be shown (Bretherton, 1987) that the buoyancy function follows very closely a piecewise-linear profile. Thus, the following mapping is used to close (1)

$$\frac{b^e(\chi)}{b_1}=-\frac{D}{\chi_s}\chi+\left(\frac{1+D}{1-\chi_s}+\frac{D}{\chi_s}\right)\delta_s\ln\left[\exp\left(\frac{\chi-\chi_s}{\delta_s}\right)+1\right] \tag{3}$$

This function corresponds to a first-order derivative following a hyperbolic tangent between two different levels and centered at the value χ_s that indicates saturation conditions.

Table 1: Simulation series: lower layer total-water specific humidity $q_{t,0}$ and temperature T_0. Buoyancy reversal parameter D defined by equation 4. Pressure level 940 hPa and upper layer at 19.1 °C and $q_{t,1}$=1.50 g kg^{-1}.

	$q_{t,0}$ (g kg^{-1})	T_0 (°C)	D	χ_s	χ_c
A0	8.0	10.5	-	-	-
A1	9.0	10.6	0.031	0.09	0.12
A2	10.0	10.8	0.074	0.22	0.27
A3	12.0	11.3	0.133	0.39	0.46

The parameter $b_1=g(\rho_0-\rho_1)/\rho_0$ quantifies the strength of the stable inversion, and the minimum buoyancy b_s is written in terms of the buoyancy reversal parameter

$$D=\frac{\rho_s-\rho_0}{\rho_0-\rho_1}=-\frac{b_s}{b_1} \tag{4}$$

This mapping $b^e(\chi)$ is shown in figure 1. The interval of mixture fraction between $\chi=0$ and the cross-over value $\chi_c=(\chi_s+D)/(1+D)$ where the buoyancy is negative represents a region of buoyancy reversal, in this case due to evaporative cooling. The curves in that figure correspond to the data shown in table 1. Case A1 is taken from field measurements in nocturnal marine stratocumulus in the DYCOMS-II study (Stevens et al., 2003); case A0 does not have buoyancy reversal, with a linear relation between b and χ; cases A2 and A3 have stronger buoyancy reversal than A1 but the same inversion value b_1.

This hypothesis of phase equilibrium does equally not hold in the real atmospheric case. The time-scales associated with the evaporation of cloud droplets with a diameter of 10 μm is of the order of several seconds (Shaw, 2003), which might be comparable to the integral time-scales of the small-domain system that we are considering, as we will see later. Larger systems do indeed have longer times, but the corresponding Kolmogorov scales remain small compared to evaporation times.

It is worth noting that the cloud-top problem formulation written in terms of the mixture fraction as shown here is formally similar to the infinitely-fast reacting flow that develops between two parallel streams, except for the inertial effects in the latter due to the strong density variation (Peters, 2000; Pantano et al., 2003).

If there is no velocity-scale externally imposed, then dimensional analysis shows that b_1 and a reference length-scale L_0 can be used to write the general solution as

$$\begin{aligned}\frac{\mathbf{v}(\mathbf{x},t)}{\sqrt{L_0 b_1}} &= f(\frac{\mathbf{x}}{L_0},t\sqrt{\frac{b_1}{L_0}};Gr,Pr,\chi_s,D,\frac{a}{L_0},\frac{\delta}{L_0})\\ \chi(\mathbf{x},t) &= g(\frac{\mathbf{x}}{L_0},t\sqrt{\frac{b_1}{L_0}};Gr,Pr,\chi_s,D,\frac{a}{L_0},\frac{\delta}{L_0})\end{aligned} \tag{5}$$

which introduces the reference Grashof number $Gr=L_0^3 b_1/\nu^2$ and the Prandtl number $Pr=\nu/\kappa$. The parameters a and δ describe the geometry of the initial condition and they are later explained.

The system of transport equations formed by (1) and (3) are solved numerically following the incompressible algorithm presented by Wilson et al. (1998). We employ sixth-order compact schemes for the first- and second-order spatial derivatives, involving the resolution of tridiagonal linear systems, and a fourth-order Runge-Kutta scheme for the

time advancement. The Poisson equation is written using Fourier decomposition along the horizontal periodic planes parallel to xOy to reduce it to a sequence of one-dimensional second-order equations. However, further simplification is needed because the matrix of each of the resulting linear systems is full and therefore the exact resolution of them is computationally too demanding. We substitute the two first-order finite-difference operators by one second-order finite difference (Wilson et al., 1998; Cook and Dimotakis, 2001), which leads to a pentadiagonal system. It has been shown (Mellado et al., 2009) that the associated truncation error, which introduces a non-zero dilatation, can be small enough for the study of large-scale statistics using an adequate resolution. The boundary conditions at the top and the bottom are no-penetration free-slip boundary conditions, although tests are always performed to assure no influence of these constraints on the data analyzed.

BUOYANCY REVERSAL INSTABILITY

As explained before, the cloud-top mixing layer is described in terms of a dry and warm top layer where $\chi = 1$ and a moist and cold bottom layer where $\chi = 0$. If motion is absent, both regions mix due to molecular diffusion and the inversion evolves towards an error function profile

$$\chi_i(z) = \frac{1}{2}\left[1 + \mathrm{erf}\left(\frac{z}{2\delta}\right)\right] \tag{6}$$

where δ parameterizes the thickness. This two-layer structure in the mixture fraction leads to a three-layer structure in the density, as shown in figure 2, due to the nonlinear mapping $b^e(\chi)$ shown in figure 1 and expressed in (3). This configuration is linearly unstable and the associated instability is the *buoyancy reversal instability*. In the single-mode numerical simulations performed to illustrate this instability, the system is perturbed by displacing sinusoidally the central isosurface of χ over a wavelength λ with an amplitude $(a/2)$, so that a characterizes the initial thickness of the mixing layer. This initial condition can be expressed as

$$\chi(\mathbf{x}, 0) = \chi_i(z + \zeta) = \frac{1}{2}\left[1 + \mathrm{erf}\left(\frac{z+\zeta}{2\delta}\right)\right] \tag{7}$$

and $\zeta(x) = (a/2)\cos(2\pi x/\lambda)$. In the cases presented in this section, the values $(a/2)/\lambda = 0.1$ and $\delta/\lambda = 0.025$ are used. The wavelength λ is taken as the reference length-scale L_0, and the reference Grashof number in the simulations here discussed is $Gr = 6.4 \times 10^9$. The Prandtl number is $Pr = 1$. A uniform grid 512×1024 provides enough resolution for this problem with the numerical scheme described in the previous section. A common reference for the sixth-order compact scheme is about 6 points per gradient thickness

$$\delta_\chi(t) = \frac{1}{(\partial\langle\chi\rangle/\partial z)_{\max}} \tag{8}$$

which is terms of the the error function profile χ_i is $\delta_{\chi,0} \simeq 3.54\delta$. However, we need to resolve here the layer of negative buoyancy ($\chi < \chi_c$), and that explains the value $\delta/\lambda = 0.025$ so that $\chi_c\delta_{\chi,0}/\Delta z > 5$.

Details about the linear stability analysis, the simulation and the flow that develops from this initial condition have been discussed in Mellado et al. (2009). The main characteristic of the system, as already mentioned, is that the two-layer structure in the mixture fraction (i.e. enthalpy and total-water specific humidity) corresponds to a three-layer system in terms of the density, with the central one heavier than the lower one. Linear stability analysis shows

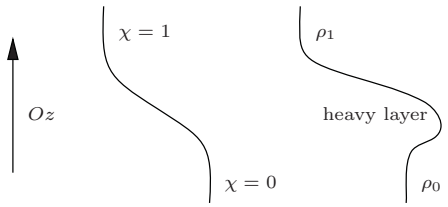

Figure 2: Sketch showing the two-layer vertical structure in terms of the mixture fraction χ and the associated three-layer structure in the density, with a middle heavier layer in case of buoyancy reversal.

that, in the case $D \ll 1$ typical of stratocumulus tops, this configuration has one stable mode of period $2\sqrt{\pi}\sqrt{\lambda/b_1}$ (or two dispersive waves with phase velocity $\sqrt{\lambda b_1/(4\pi)}$) and one unstable mode with a characteristic time-scale $D^{-1/2}$ times larger than the stable one. The system is then linearly unstable and the corresponding buoyancy reversal instability can lead to a turbulent flow in the lower layer similar to that generated in Rayleigh-Bénard convection.

Figure 3 presents the negative buoyancy reversal field (points $\mathbf{x}$ for which $b(\mathbf{x}, t) < 0$ are visualized using a gray scale, white for zero and black for minimum buoyancy b_s) and shows the initial condition, in the form of a single-mode perturbation, and the state for each case A0-A3 after an interval of time equal to 4 times the period of the inversion oscillation according to linear theory, $2\sqrt{\pi}\sqrt{\lambda/b_1}$. The stable case A0 is represented by $b^e(\chi(\mathbf{x}, t)) < 0$ using the function $b^e(\chi)$ corresponding to case A1 in order to compare the flow structure of both. The box height shown is only the lower 3/4 of the domain employed in the simulation, and in case A3 a longer domain in the vertical direction, a grid 512×1280, has been used to avoid the influence of the lower boundary. All four simulations are out of phase after the four periods due to nonlinear effects at the interface that modify the period of oscillation of the standing interfacial gravity wave of the inversion. On top of this oscillation, a downdraft forms in the cases A1-A3 with buoyancy reversal, and the falling speed of this downdraft increases as the evaporative cooling is augmented, as expected. This finger develops a mushroom shape characteristic of the Rayleigh-Taylor problem for small density differences. This figure also shows the convoluted mixing pattern that forms due to buoyancy reversal even for the low values of D characteristic of atmospheric conditions. This result suggests that a full turbulent flow can develop in the lower layer, not only a weak recirculation as suggested in the past (Siems et al., 1990; Siems and Bretherton, 1992).

TURBULENT FLOW

A three-dimensional simulation of the system in case A1 on a cubic domain of size L_0^3 has been performed using a grid size 1024^3. The initial condition is set as before using (7), with a thickness $\delta/L_0 = 0.0125$. The plane defined by the isosurface $\chi_i = 0.5$ ($z = 0$) of the background inversion is positioned at 3/4 of the vertical direction; preliminary simulations (not shown) confirm that there is no influence from the upper boundary. However, the cross-over value of the mixture fraction χ_c can be used to define a possibly more relevant reference inversion plane at

$$z_i = 2\delta\,\mathrm{erf}^{-1}(2\chi_c - 1) \tag{9}$$

where erf^{-1} indicates the inverse error function. This iso-

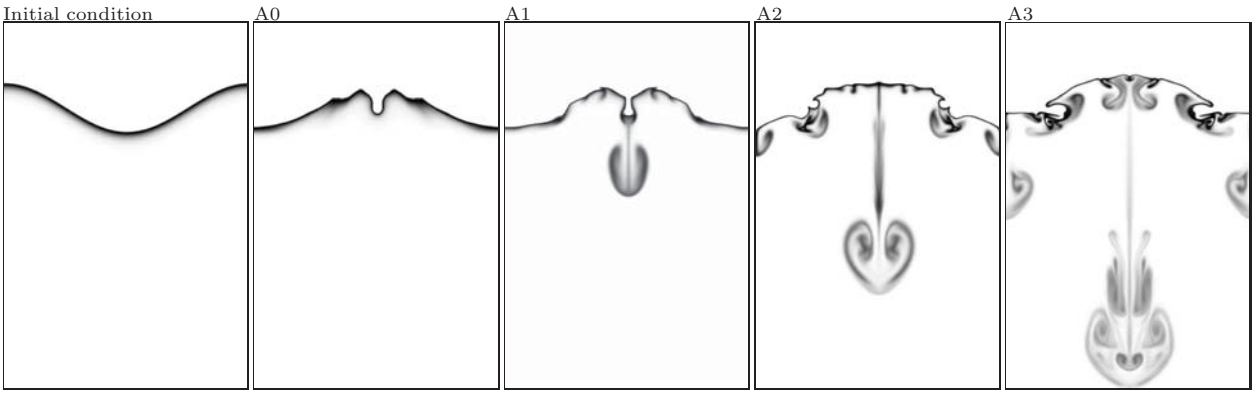

Figure 3: Negative buoyancy field after four periods $2\sqrt{\pi}\sqrt{\lambda/b_1}$ of the linearly stable mode starting from the single-mode initial condition (left figure). The reference Grashof number is $Gr = 6.4 \times 10^9$.

surface partitions the system into positively ($\chi > \chi_c$) and negatively ($\chi < \chi_c$) buoyant mixtures (see figure 1). For the current simulation, $z_i/L_0 = -0.02$. The initial condition is further prescribed by specifying a random broadband vertical displacement $\zeta(x, y)$ of the central interface $\chi = 0.5$. The power spectral density of ζ corresponds to a Gaussian function centered at $1/\lambda = 1.5/\delta_{\chi,0}$ and with a standard deviation equal to $1/(6\lambda)$, so that there is practically no energy for spatial frequencies below $1/(2\lambda)$. The phase of ζ is random. The root-mean-square (r.m.s.) of this function is $\zeta_{\rm rms}/\lambda = 0.15$; in this turbulent case, the parameter a is defined as $a = 2\zeta_{\rm rms}$. This set-up follows the initializations used in simulations of Rayleigh-Taylor turbulence (Cook and Dimotakis, 2001; Mellado et al., 2005). Note that these values lead to ratios δ/λ significantly larger than those prescribed in the single-mode studies, but the aim in this initial condition is to promote the development of a fully turbulent state, and a rapid and strong multimode interaction is therefore preferable to a detailed representation of the transition between the linear and the non-linear regimes. The same Grashof number $Gr = 6.4 \times 10^9$ as in the two-dimensional cases is employed and $Pr = 1$.

In this section, the nondimensional results are presented in terms of L_0 and b_s instead of b_1, because it is the former quantity that better characterizes the turbulent fields in the lower layer. Thus, statistics constructed using averages along horizontal planes will depend on the vertical distance z/L_0 and on the nondimensional time

$$\tau = t\sqrt{|b_s|/L_0} \tag{10}$$

Figure 4 depicts qualitatively the evolution of the turbulent flow by means of the negative buoyancy field at three times, using again a gray scale ranging from zero buoyancy (white) to b_s (black). Several points should be appreciated. First, a turbulent flow seems to develop in the lower layer, in the sense that there is a three-dimensional vorticity fluctuation (inferred from the fluctuation of b shown in that figure and confirmed by vorticity statistics not shown here) over a broadband range of scales. The forcing is to be found in the vertical downdrafts of cool fluid that develop between the domes observed at the inversion, which suffer then shear instabilities and transfer turbulent energy to the horizontal motion. Last, the inversion remains relatively thin and its mean position is not significantly displaced in the vertical direction. This flow configuration is very reminiscent of the penetrative convection that forms when a stable stratification over a horizontal boundary is heated from below (Fernando and Little, 1990), here the system being upside-down.

Quantitatively, the evolution of the flow is described first in terms of the mixture fraction, presenting mean and fluctuation profiles in figures 5 and 6, respectively. The mean profile $\langle\chi\rangle$ shows the penetration of the mixing region into the neutrally-stable lower layer. The mean values of mixture fraction inside the mixing region are small compared to the inversion value, even smaller than the cross-over value $\chi_c = 0.12$, and the evolution is only clearly observed in the inset of figure 5. On the other hand, the inversion remains located at about the initial position $z = 0$, with a small thickening towards the upper layer consistent with the conservation property of the mixture fraction, and seemingly dominated by diffusion processes.

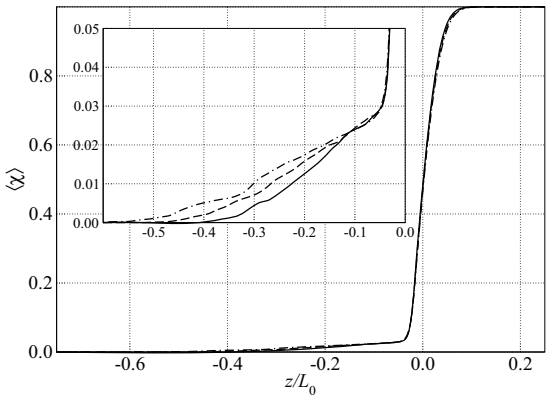

Figure 5: Mean profile of mixture fraction for case A1 at different times: $\tau_1 = 4.03$, solid; $\tau_2 = 4.70$, dashed; $\tau_3 = 5.40$, dot-dashed. The cross-over mixture fraction separating negatively from positively buoyant mixtures is $\chi_c = 0.12$.

The fluctuation of the mixture fraction is illustrated by figure 6, where the profile of the r.m.s. is plotted. There are at least two regions to be distinguished. First, there is a broad zone below $z/L_0 \simeq -0.1$, corresponding to the turbulent region, with fluctuation values about 1%; compared with χ_c, the value that seems to cap the turbulent motion at the inversion, that turbulence intensity is of the order of 10%. Second, there is a strong peak of $\chi_{\rm rms}$ at about $z/L_0 \simeq -0.02$, which does not vary strongly in time

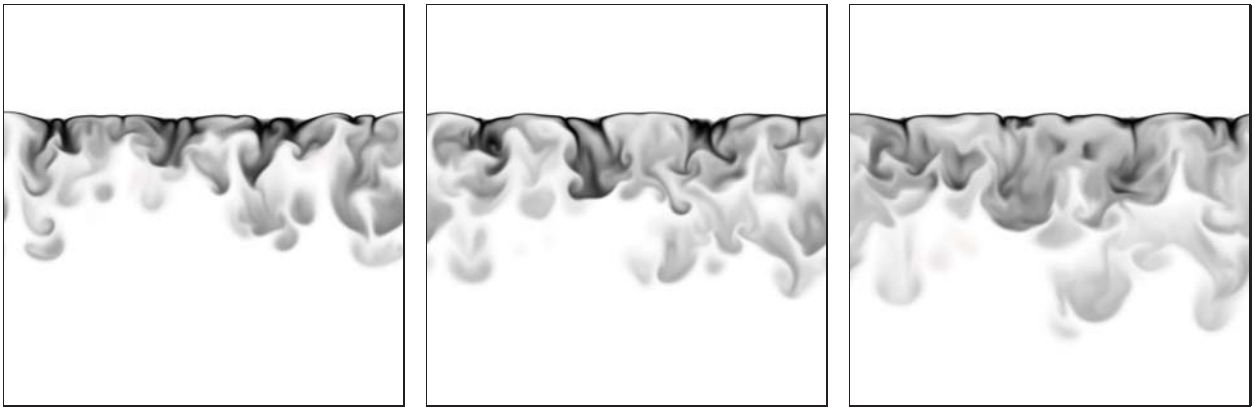

Figure 4: Evolution (left to right) of the negative buoyancy field for case A1 starting from broadband initial conditions. Vertical planes at times $\tau_1 = t\sqrt{L_0/b_s} = 4.03$, $\tau_2 = 4.70$ and $\tau_3 = 5.40$ are shown. The reference Grashof number is $Gr = 6.4 \times 10^9$.

and that approximately corresponds to the point of maximum mean gradient observed in figure 5. The location of this maximum gradient is not at $z = 0$ because the problem is asymmetric, and it is more related to the position of the reference inversion plane z_i introduced before in (9) and based on the initial background profile and the cross-over value χ_c. This inflexion point separates positive curvature below it, and therefore mean molecular diffusion increasing $\langle\chi\rangle$, from convexity above it, and therefore mean molecular diffusion decreasing $\langle\chi\rangle$. The associated strong maximum in $\chi_{\rm rms}$ represents the oscillation of the stable inversion.

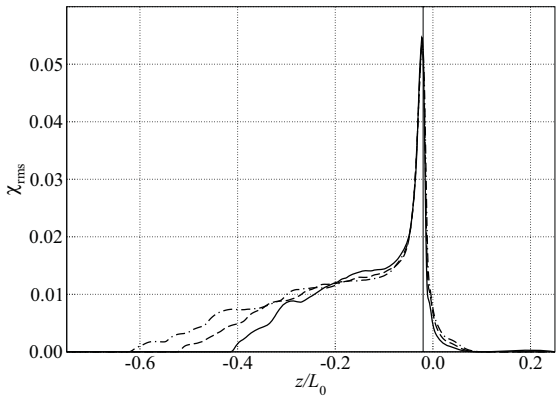

Figure 6: Mixture fraction fluctuation at different times. Same legend as in figure 5. Vertical line indicates the position of the reference inversion plane $z_i/L_0 = -0.02$, equation (9).

In terms of the velocity, the mean is zero due to the statistical homogeneity along the horizontal planes and the solenoidal character of the velocity field. The velocity turbulence intensity $\sqrt{2k}$, k being the turbulent kinetic energy per unit mass, is plotted in figure 7, nondimensionalized with the potential energy per unit mass $|b_s|L_0$ related to the saturation buoyancy b_s and the length-scale L_0. The turbulent kinetic energy continuously increases, due to the positive turbulent buoyancy flux (not shown) generated by the downdrafts, and this growth is in magnitude as well as in broadening towards the lower layer. The flow is anisotropic, with a ratio between the vertical velocity fluctuation to the horizontal one about 1.3 in the middle of the turbulent zone. The Taylor-scale Reynolds number is $Re_\lambda = w'\lambda_z/\nu \simeq 65$, where w' is the vertical velocity r.m.s. and the Taylor microscale is $\lambda_z = w'/\sqrt{\langle(\partial w'/\partial z)^2\rangle}$. The turbulent Richardson number is large, $Ri_t = b_1 k^{1/2}/\epsilon \simeq 300$, with ϵ the average turbulent dissipation rate, which explains why the turbulent zone is constrained by the inversion on top, as observed again in figure 7.

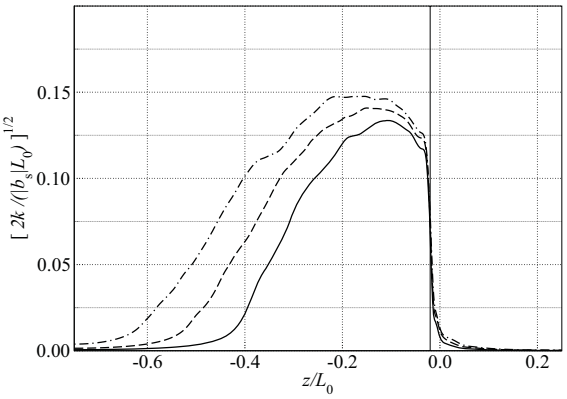

Figure 7: Turbulent kinetic energy at different times. Same legend as in figure 6.

These results are now briefly discussed in terms of dimensional quantities and in the context of stratocumulus tops. The reference case A1 from the DYCOMS-II field measurements corresponds to an inversion buoyancy $b_1 = 0.25$ m s^{-2}, and therefore a minimum reversal buoyancy (at saturation) $b_s = -0.031 b_1 = -7.75 \times 10^{-3}$ m s^{-2}. This value of b_1 implies that the reference Grashof number $Gr = 6.4 \times 10^9$ used in this work corresponds to atmospheric conditions for a reference length-scale L_0 of about 2 m, calculated using a kinematic viscosity of 1.5×10^{-5} m^2 s^{-1}. The corresponding reference time-scale $\sqrt{L_0/|b_s|}$ is about 16 s, and that associated with the restoring force of the inversion is $\sqrt{L_0/b_1} \simeq 3$ s, much shorter. As mentioned before, these values are comparable to the times-scales of droplet evaporation, and therefore the assumption of thermodynamic equilibrium is not fulfilled. (One could hypothesize that finite rate effects would make the flow to develop slower.)

The reference velocity is $\sqrt{|b_s|L_0} \simeq 12$ cm s^{-1}. Hence, the characteristic fluctuation velocity $\sqrt{2k}$ calculated from figure 7 is about 2 cm s^{-1}. This velocity is more than

one order of magnitude smaller than those measured by Caughey et al. (1982), who report velocity fluctuations of 1 m s^{-1} right below the cloud top. This is consistent with the thought that the buoyancy reversal cannot compete with the stronger turbulent state imposed by the large-scale motion inside the whole planetary boundary layer (Yamaguchi and Randall, 2008). At the same time, the results here presented show that turbulent entrainment of upper layer fluid only due to buoyancy reversal effects is not predominant because the corresponding Richardson numbers are too large for the turbulent motion in the lower layer to break through the inversion, and thus they suggest that buoyancy reversal *alone* cannot be responsible for the cloud deck break-up.

In summary, the three-dimensional simulations reported in this section confirm the scenario suggested by the stability analysis and the single-mode simulations of Mellado et al. (2009) and show that a turbulent flow can develop due to the buoyancy reversal instability, even for the low values $D \simeq 0.05$ characteristic of the atmospheric conditions and for the small domains considered in this DNS, of the order of 2 m. The turbulent mixing promoted by the buoyancy reversal is mainly restricted to the lower layer, it is capped and constrained by the relatively strong inversion and there is no intense engulfment of the upper laminar layer into the mixing region, the mixing zone broadens predominantly downwards. The required thickening of the vertical profile $\langle\chi\rangle$ upwards due to the conservation of χ seems to occur mainly in a laminar diffusion fashion. Hence, it seems more reasonable to consider the possible effects of buoyancy reversal as a modification to an already existing turbulent entrainment process at the cloud top caused by the turbulent state of the boundary layer below or by local mean shear. The application of the results obtained from this simplified analysis to the real situation found in stratocumulus tops is limited, because the presence of a continuous external forcing due to the turbulent state of the lower layer is not considered here (in addition, of course, to the departures from the two-fluid and equilibrium hypotheses).

CONCLUSIONS

The buoyancy reversal instability occurring in the cloud-top mixing layer due to evaporative cooling has being introduced and the subsequent flow described using direct numerical simulation. A physical model based on a mixture fraction has been used as in previous works, investigating the role of latent heat effects at the cloud top. Single-mode cases have illustrated the non-linear evolution of the instability, previously identified by linear analysis. A three-dimensional simulation using a broadband random initial perturbation of the inversion has shown the turbulent state that can develop even for the cases of weak buoyancy reversal typical of atmospheric conditions at the stratocumulus clouds. This turbulent zone grows with time into the lower layer, the turbulent kinetic energy continuously increasing, but it is strongly capped by the stable inversion. More detailed characterization of the turbulent state, possibly in terms of a self-similar evolution, is currently under investigation.

Partial financial support for this work was provided by the Deutsche Forschungsgemeinschaft within the SPP 1276 Metström program.

REFERENCES

Bretherton, C. S., 1987. "A theory for nonprecipitating moist convection between two parallel plates. Part I: Thermodynamics and linear solutions." *J. Atmos. Sci.*, 44:1809–1827.

Caughey, S. J., Crease, B. A., and Roach, W. T., 1982. "A field study of nocturnal stratocumulus II Turbulence structure and entrainment". *Q. J. Roy. Meteorol. Soc.*, 108:125–144.

Cook, A. W. and Dimotakis, P. E., 2001. "Transition stages of Rayleigh-Taylor instability between miscible fluids". *J. Fluid Mech.*, 443:69–99.

Fernando, H. J. S. and Little, L. J., 1990. "Molecular-diffusive effects in penetrative convection". *Phys. Fluids A*, 2(9):1592–1596.

Kuo, H. and Schubert, W. H., 1988. "Stability of cloud-topped boundary layers". *Q. J. Roy. Meteorol. Soc.*, 114:887–916.

Kurowski, M. J., Malinowski, S. P., and Grabowski, W., 2009. "A numerical investigation of entrainment and transport within a stratocumulus-topped boundary layer". *Q. J. Roy. Meteorol. Soc.*, 135:77–92.

Lilly, D. K., 1968. "Models of cloud-topped mixed layers under strong inversion". *Q. J. Roy. Meteorol. Soc.*, 94:292–309.

Mellado, J. P., Sarkar, S., and Zhou, Y., 2005. "Large-eddy simulation of Rayleigh-Taylor turbulence with compressible miscible fluids". *Phys. Fluids*, 17:076101.

Mellado, J. P., Stevens, B., Schmidt, H., and Peters, N., 2009. "Buoyancy reversal in cloud-top mixing layers". *Q. J. Roy. Meteorol. Soc.*

Pantano, C., Sarkar, S., and Williams, F. A., 2003. "Mixing of a conserved scalar in a turbulent reacting shear layer". *J. Fluid Mech.*, 481:291–328.

Peters, N., 2000. *Turbulent combustion*. Cambridge University Press.

Randall, D. A., 1980. "Conditional instability of the first kind upside-down". *J. Atmos. Sci.*, 37:125–130.

Shaw, R. A., 2003. "Particle-turbulence interactions in atmospheric clouds". *Annu. Rev. Fluid Mech.*, 35:183–227.

Shy, S. S. and Breidenthal, R. E., 1990. "Laboratory experiments on the cloud-top entrainment instability". *J. Fluid Mech.*, 214:1–15.

Siems, S. T. and Bretherton, C. S., 1992. "A numerical investigation of cloud-top entrainment instability and related experiments". *Q. J. Roy. Meteorol. Soc.*, 118:787–818.

Siems, S. T., Bretherton, C. S., Baker, M. B., Shy, S., and Breidenthal, R. E., 1990. "Buoyancy reversal and cloud-top entrainment instability". *Q. J. Roy. Meteorol. Soc.*, 116:705–739.

Stevens, B., 2002. "Entrainment in Stratocumulus-topped mixed layers". *Q. J. Roy. Meteorol. Soc.*, 128:2663–2690.

Stevens, B., D-H-Lenschow, Faloona, I., Moeng, C. H., Lilly, D. K., Blomquist, B., Vali, G., Bandy, A., Campos, T., Gerber, H., Haimov, S., Morley, B., and Thorton, C., 2003. "On entrainment rates in nocturnal marine Stratocumulus". *Q. J. Roy. Meteorol. Soc.*, 129(595):3469–3493.

Wilson, R. V., Demuren, A. O., and Carpenter, M., 1998. "Higher-order compact schemes for numerical simulation of incompressible flows". Technical Report CR-1998-206922, NASA Langley Research Center.

Yamaguchi, T. and Randall, D. A., 2008. "Large-eddy simulation of evaporatively driven entrainment in cloud-topped mixed layers". *J. Atmos. Sci.*, 65:1481–1504.